Amorphous calcium organophosphates nanoshells as potential carriers for drug delivery to Ca^{2+}-enriched surfaces.

Darlin J. Perez Enriquez,[†] **María L. Dell' Arciprete,**[†,*] **María L. Dittler,**[†] **Alejandro Miñan,**[†] **Eduardo Prieto,**[†] **and Mónica C. Gonzalez**[†]

† Instituto de Investigaciones Fisicoquímicas Teóricas y Aplicadas (INIFTA), CCT-La Plata-CONICET, Universidad Nacional de La Plata, La Plata, Argentina. Diagonal 113 y 64, La Plata, Argentina.

ABSTRACT

A highly selective nanocarrier for targeted drug transport and delivery to calcium-containing surfaces, as bone mineral matrix, is described. The nanocarrier, a calcium phosphate (CaP) nanoshell, is capable of interacting with calcium ions contained in enriched surfaces (Ca^{2+} modified mica surface, hydroxyapatite nanoparticles (Ap) films on glass, and Ap modified 45S5® bioactive glass-based scaffolds) with the consequent disruption of the inorganic structure and release of (bio) molecules contained in the interior. The antibiotic Levofloxacin (LX) was used as a model drug for the encapsulation and drug release studies which allowed monitoring by fluorescence spectroscopic methods. Accumulation and disruption of CaP nanoshells triggered by calcium ions over surfaces, was followed by microscopy techniques as SEM, AFM, and fluorescence microscopy. Bacterial susceptibility and time killing assays demonstrated the bactericidal potential of the nanoshells containing LX. A mechanism for the Ca^{2+}-activated CaP nanoshell accumulation and drug release is

1

24 proposed and discussed.

25

28

1. INTRODUCTION

30 The development of delivery systems for drugs, proteins, DNA and genes, among others, represents

31 an accepted and essential strategic tool for the treatment of illness. It addresses issues associated with

32 pharmaceuticals solubility and stability in the biological environment, maintenance of the drug

33 effective concentration, enhanced drug performance and acceptability by increasing efficacy,

34 improving safety and patient compliance.[1,2] To meet the requirements of an effective drug delivery,

35 vehicles are designed to control drug release at a desired target site as response of an internal or external

36 stimuli. Internal stimuli-responsive nanocarriers release their cargo as a consequence of the specific

37 physicochemical characteristics of the physiological targeted site as pH, redox and thermal conditions,

38 and the presence of specific enzymes.[3] Nanoparticles of various compositions as calcium phosphate,

39 gold, bioglass, polymer-modified porous silicon, natural polymers as chitosan and elastine, and

40 liposomes, are among the drug nanocarriers developed to stimulate mineralization and/or promote

41 osteoblast activity in bone tissue.[4–6] Drug delivery to bone is limited by the tissue characteristics

42 composed by the nanoscale ensemble of minerals (~ 69%) and organic matrix, being hydroxyapatite

43 the principal component. The local pH diminution and the increase of Ca^{2+} concentration taking place

44 during bone resorption were considered as internal boost for drugs release.[7] In that sense, the increased

45 solubility of CaP materials with a pH decrease motivated their use as pH-responsive carriers for drug

46 delivery.[8]

2

47 Liposomes comprise one of the most effective first generation nanocarriers due to their intrinsic

48 composition and ability to encapsulate hydrophilic drugs in the aqueous core or hydrophobic molecules

49 in the lipid bilayer. To overcome their poor mechanical stability and associated burst release, they were

50 coated with calcium phosphates shells (CaP). [9,10] In fact, calcium phosphate materials have received

51 much interest in the field of drug delivery due to their excellent biocompatibility and biodegradability

52 in biological systems, as well as the ability to promote osteoblast adhesion and osteoconductivity, [7,10–

53 13] at the time it provides the nanocarrier of a surface capable of being functionalized for active

54 targeting.[8]

55 In the aim of designing a bone responding nanocarrier, we evaluated the response of carboxylic-

56 functionalized calcium phosphate (CaP) coated 1,2-dioleoyl-sn-glycero-3-phosphate (DOPA)

57 liposomes [10] herein denoted CaPLi, towards Ca^{2+} enriched surfaces. To that purpose, the encapsulation

58 and delivery of the third generation fluoroquinolonic antibiotic Levofloxacin (LX) was examined.

59 CaPLi vehicles carrying the antibiotic LX are denoted CaPLiLX. Fig. 1 shows a scheme of the

60 developed LX-loaded nanocarrier system.
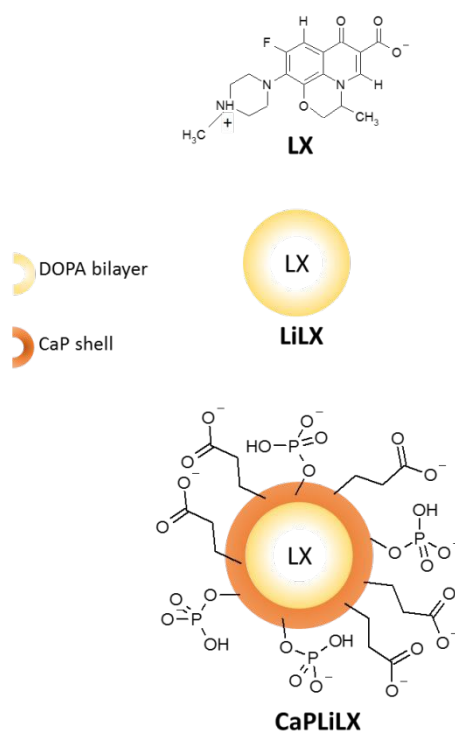
61

62 **Fig. 1.** Chemical structure of Levofloxacin (LX) and schematic representation of the nanocarrier.

2. EXPERIMENTAL SECTION

2.1 Materials.

Lyophilized lipids 1,2-dioleoyl-sn-Glycero-3-Phosphate (DOPA, Avanti Polar Lipids, Alabaster, Alabama, USA), Levofloxacin (LX, Sigma-Aldrich, St Louis, MO, USA), Acridine orange (AO, Sigma, St Louis, MO, USA), Calcium chloride (analytical grade, Anedra), Calcium hydroxide (98.5%, Sigma Aldrich), Sodium hydroxide (ACS, Cicarelli), Phosphoric acid (85%, Cicarelli), 2-Carboxyethanephosphonic acid (CEPA, 94%, Aldrich), Potassium Chloride (ACS, Biopack), Potassium Bromide (ACS, J.T. Baker), Sodium chloride (ACS, Anedra), Potassium phosphate dibasic (99%, Cicarelli), Chloroform (99.9%, J.T. Baker), Iron chloride (98.3%, J.T. Baker), Ammonium thiocyanate (97.5%, Cicarelli), Polyvinyl alcohol (PVA, completely hydrolyzed, MW 30000, Merck.), 45S5® and Bioactive glass (BG) commercial powder (particle size 4 μm $Na_2Ca_2Si_3O_9$, SCHOTT Ag, Standort Landshut) were used as obtained. All solutions were prepared in ultrapure water (0.055 μS cm^{-1}) obtained from an OSMOION™ purification system. Regenerated cellulose dialysis membrane Spectra/Por 1 with a MWCO of 6000-8000 Da was obtained from Spectrum Labs. For scaffolds preparation fully reticulated polyester-based Polyurethane (PU) foam with 60 ppi (pores per inch) from Deutschland (Eurofoam GmbH) was used as sacrificial template for the replication method.[14] The foam was cut in cylindrical shape with 12 mm of diameter and 7 mm in thickness.

2.2 Synthesis of Materials.

Bioactive glass-ceramic scaffolds (BGS) and *hydroxyapatite nanoparticles* (Ap) were obtained as described elsewhere.[15] Briefly, scaffolds were prepared by the polyurethane foam method using commercial 45S5 BG® particles. Hydroxyapatite nanoparticles were obtained by a wet chemical procedure using H_3PO_4 and calcium hydroxide as reactants. Surface modification of the scaffold was performed by deep-coating as described by Dittler *et al*.[15] The modified scaffolds were named Ap-BGS.

87 *Calcium phosphate nanoshell* synthesis was performed as described in the literature with some

88 modifications.[10] To that purpose, aqueous solutions of DOPA (1 mg/mL) and alternatively LX (100

89 µM or 6 µM, the latter for fluorescence measurements only) or AO (100 µM) were prepared and

90 homogenized by vortexing until complete dissolution. The mixture was submitted to 5 cycles of 30

91 seconds work of tapered probe sonication at 10 W with 30 second rest. Liposome formation after

92 sonication was suggested by a change in the opalescence of the suspension. [16] The sample was purged

93 with Ar for 30 minutes in an ice bath and centrifuged at 12000 rpm for 5 minutes. Samples were

94 labelled as LiLX or LiAO for LX-containing and AO-containing liposomes, respectively.

95 Coating of LiLX and LiAO with CaP and surface derivatized with 2-carboxyethanephosphonic acid to

96 yield CaP-coated liposomes labeled CaPLiLX and CaPLiAO, respectively, was performed according

97 to the protocol previously described[10] which considered the formation of a Ca^{2+} deficient calcium

98 phosphate material. Nanoshells were stored in a dark vessel at 4 °C. Fig. 1 shows the schematic

99 representation of the nanocarriers synthetized.

100 *2.3 Characterization Methods.*

101 Nanoshell formation and surface characterization were assessed by Wide Angle X-Ray Scattering

102 (WAXS), X-Ray Diffraction (XRD), Transmission electron Microscopy (TEM), High Resolution

103 Scanning Transmission Electron Microscopy (HR-STEM), Energy Dispersive X-ray Spectroscopy

104 (EDS), ATR-FTIR spectroscopy, dynamic light scattering (DLS) and electrophoretic mobility (μ_e),

105 as described in S.I. "Characterization Methods". *Photoluminescence measurements* for CaPLiLX

106 characterization were performed using a Jobin-Yvon Spex Fluorolog FL3-11 also described in the

107 supporting information.

108 *Lipid quantification* of LiLX was accomplished by Stewart colorimetric assay.[17] The lipid

109 concentration on 1:10 diluted LiLX sample measured by Stewart method yielded a concentration of

110 the order of 0.1 mg/mL, indicating that all the DOPA initially incorporated during synthesis was

111 forming vesicles.

Calcium quantification in CaPLiLX suspension was determined by ICP-OES using a Shimadzu, ICPE-9820 instrument. The quantitative determination was performed according to EPA 6010.

LX encapsulation efficiency (EE%) of LX in the liposomes was determined as the ratio between the emission intensity upon 330 nm excitation of LX in DOPA mixtures right after vortexing and sonication (C_{LXini}) and that after liposome dialysis against ultrapure water for 24 h (C_{LXlipo}), EE% = $100 \times C_{LXlipo}/C_{LXini}$. The strategy used for the determination of the encapsulation efficiency minimizes the effects of light scattering and fluorescence quenching due to the presence of liposomes. However, since no other correction was performed, the obtained EE% is a lower limit value.

2.4 Drug release studies.

The release profiles of LX were investigated in PBS (pH 7.4) and acetate (pH 4.35) buffers, and in Simulated body fluid (SBF, pH 7.4) with ion concentrations nearly equal to those of human blood plasma. A volume of 3 mL CaPLiLX suspension (3.4×10^{-6}M LX after dialysis estimated from UV-vis absorption calibration curve, *see* Section 3.2 below), or alternatively 1.7×10^{-5}M LX solution, were placed in 2.7 x 4.7 cm dialysis membrane bags and immersed in 200 mL (V_0) of PBS or acetate buffers, or SBF solution. The solutions were incubated at (37 ± 1) ºC under stirring (80 rpm) up to 75 h. [18] At different time intervals, 2mL-aliquots (V_i) of the release medium were taken and replaced with the same volume of fresh media solution. The assays were performed in duplicates. The LX concentration (C_i) in the aliquots were determined by measuring the fluorescence intensity at 450 nm (PBS buffer and SBF) or 495 nm (acetate buffer) and the actual LX released concentration obtained by comparison with a fluorescence-LX concentration calibration curve in the same media. The LX release rate (RR) was calculated by $RR = (Q_n/W)$ where W is the total drug content in the original CaPLiLX samples and Q_n the cumulative released mass at each time interval n.[18] Q_n may be calculated as $Q_n = C_n \times V_0 + \sum_{i=0}^{n-1} C_i \times V_i$.

136

2.5 Interaction with surfaces.

138 Interaction of LiLX and CaPLiLX samples with Ca^{2+}- rich mica surfaces was addressed by *Atomic*

139 *Force Microscopy*. The measurement was performed in dynamic mode (tapping) thus avoiding

140 changes induced by lateral forces. In all instances, 10 µl of the samples were dropped on freshly

141 cleaved mica substrates with and without the previous addition of 10 µL of $CaCl_2$ 0.1 M. Samples

142 were dried under N_2 for 10 minutes and analyzed through the use of probes doped with silicon nitride

143 (Model RTESP, Veeco Instruments, Santa Barbara, CA, USA; tip radii, 8–12 nm, 271–311 kHz, force

144 constant 40 N m^{-1}). Images were obtained at 25ºC with a Multi-Mode Scanning Probe Microscope

145 (Veeco) equipped with a Nanoscope V controller (Veeco) at the typical scanning rate (1 Hz).

146 Interaction of CaPLiLX deposited on BGS and Ap-BGS was observed by *Scanning Electron*

147 *Microscopy* (SEM) images taken using an environmental scanning electron microscope FEI Quanta

148 200, after 10 and 120 minutes of contact. Sample preparation involved fixation and dehydration steps.

149 Fixation was performed by immersion of the slides in a 2% glutaraldehyde solution at 4ºC for 2 h and

150 washed with a PBS (pH 7.4) buffer solution. Dehydration was performed by sequential immersion in

151 cool ethanol-water mixtures (30%, 50%, 70%, 90% and 95%) followed by two immersion processes

152 in absolute ethanol at room temperature for 20 min. Samples were treated by critical point drying in

153 order to replace the liquids by CO_2 and further metalized with Au.

154 In order to confirm the nanoshell interaction with Ca^{2+} - enriched surfaces, samples carrying the dye

155 AO were prepared as described in the experimental section and observed by *epifluorescence*

156 *microscopy*. The samples were deposited over clean glass slides and Ap modified glass slides.

157 Immediately after deposition (0 min) and after 10 and 180 minutes of contact time, the surfaces were

158 observed with a fluorescence microscope (Olympus BX51, Olympus Corp., Tokyo, Japan) equipped

159 with a #WB filter (dichroic mirror DM500, excitation filter BP450-480, emission filter BA515). The

160 microscope was connected to an Olympus DP71 (Olympus Corp., Tokyo, Japan) color video camera.

161 Images were taken instantly after opening the microscope shutter to the computer monitor, and in

162 identical experimental conditions. The images were analyzed by Image J software.

163 *2.6 Bacterial studies.*

164 *Bacterial suspensions.* *S. aureus* ATCC-25923 was inoculated in 150 mL of sterile nutrient broth (NB,

165 Britania, Argentina) and grown overnight with shaking (170 rpm) at (37 ± 1) ºC. The bacterial

166 suspension was further adjusted with fresh NB to 1×10^5 bacteria/ml and used for the biological assays.

167 *Antibiotic susceptibility assay.* The minimum inhibitory concentration (MIC) of LX against planktonic

168 *S. aureus* was performed using the broth microdilution method according to the CLSI guidelines.[19]

169 The MIC was defined as the lowest concentration of LX at which bacterial growth was not detected

170 after 20 h. The minimum bactericidal concentration (MBC) of LX for planktonic bacteria was

171 determined by plate count method. The antibiotic concentration that produced 99.9% mortality was

172 considered as the MBC. The assays were performed in triplicates from independent bacterial cultures.

173 *In Vitro Time-Kill Experiment.* Static time-kill studies were conducted to evaluate the antimicrobial

174 activity of LX-containing nanoshells according to a previously reported method.[20] All experiments

175 were performed with an initial *S. aureus* inoculum of $\sim 5.0 \times 10^4$ bacteria/mL at (37 ± 1) ºC. Time-kill

176 assays were performed in duplicate using CaPLiLX suspension and LX solution at 2x MIC (MBC, 1.0

177 µg/mL). At defined time intervals (0, 3, 6, 24 h), bacterial growth was quantified by plating 10-fold

178 dilutions on nutrient agar (Britania, Argentina). Moreover, growth control was performed and

179 consisted of a bacterial suspension with fresh NB which was enumerated in the same time interval.

180 Finally, viable bacteria values were plotted against time for each formulation.

181

3. RESULTS AND DISCUSSION

183 *3.1 Characterization of CaPLiLX samples.*

8

184 HR-STEM, TEM, and SEM electron microscopy images of CaPLiLX samples (*see* Fig. 2a and b and

185 S.I., Fig. S1) showed polydisperse spherical-shaped nanoparticles of 90-160 nm size. While a typical

186 core-shell structure is observed in the TEM image in Fig. S1c, EDS mapping images (Fig. 2c-d) show

187 the homogeneous distribution of Ca and P on the nanoshells.[21] The presence of N which could only be

188 attributed to the presence of LX is also distributed uniformly in the nanospheres (Fig. 2e), thus

189 confirming LX inclusion in CaPLiLX nanostructure. Moreover, all electron microscopy images only

190 show the presence of nanospheres before and after CaP coating, thus strongly supporting that no CaP

191 separate particles are formed.

192 The average size of 171.8 ($\pm$ 0.8) nm measured by DLS for CaPLiLX suspended in aqueous

193 suspensions is in line with the sizes observed by TEM, HR-STEM and SEM data. Therefore, a low

194 agglomeration of CaPLiLX in aqueous suspensions may be inferred. In fact, CaPLiLX average size

195 measured by DLS after one-week storage of the suspensions at 4 $^{\circ}$C is of 176 ($\pm$ 2) nm, thus also

196 suggesting a good stability of CaPLiLX suspensions.
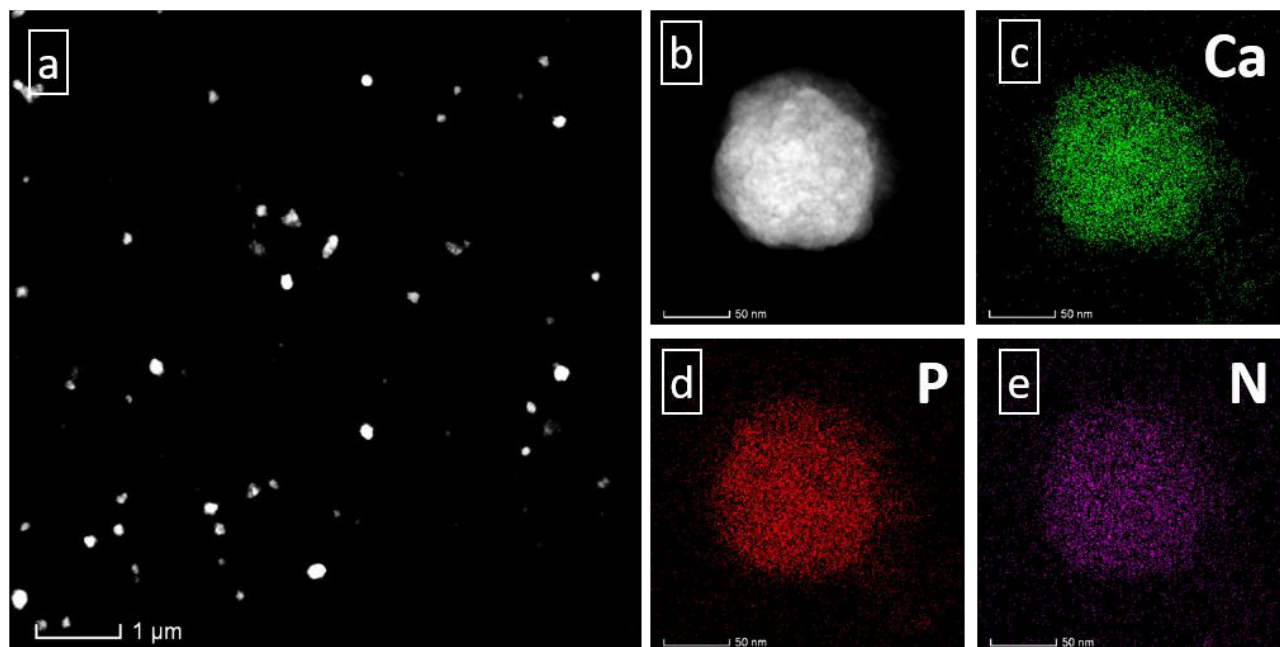

197

198

199 **Fig. 2.** HR-STEM images of CaPLiLX (a and b), EDS elemental mapping images of Ca, P and N (c,

200 d and e, respectively).

202 Fig. 3 reports the ATR-FTIR spectra of LX, DOPA, CaP nanoparticles deposited in the absence of

203 liposomes, LiLX and CaPLiLX. LiLX samples show characteristic peaks of DOPA at 1465 cm^{-1} and

204 1175 cm^{-1} assigned to -CH$_2$ scissoring and C-O symmetric stretching of esters in the lipid structure.

205 Other DOPA characteristic peaks at 2695 and 1740 cm^{-1} are also observed in LiLX samples, as

206 discussed further on. LiLX depict LX characteristic bands at 1625, 1250-1300 and 1085 cm^{-1} assigned

207 to keto oxygen in LX ring, stretching of amines and C-F group, respectively, thus confirming the

208 simultaneous presence of LX and DOPA liposomes in the samples.

209 After coating LiLX with a shell of calcium phosphate, the IR-ATR spectrum of CaPLiLX exhibited

210 bands at 896, 1060 (very intense), and 1118 cm^{-1} characteristic of the stretching vibrations of P-OH,

211 and P-O in phosphates. Characteristic DOPA bands at 2695, 1740, and 1465 (small) cm^{-1} associated

212 to HO- vibrations of O=P-OH[12] groups, stretching of ester carbonyls in lipids, and -CH$_2$ scissoring,

213 are also observed in CaPLiLX spectra. Bands associated to the asymmetric and symmetric stretching

214 of carboxylate groups[22] at 1577 and 1406 cm^{-1}, respectively, may be due to attached CEPA

215 terminations on the CaPLiLX surface. The double band at 2857-2927 cm^{-1} is assigned to C-H

216 stretching confirm the presence of carbon-chains on the nanoshell surface. Interestingly, sharp peaks

217 at 3570 cm^{-1} due to OH stretching in highly crystalline CaP powders,[23,24] is absent in CaPLiLX

218 spectrum. However, it should be noted that CaP nanoparticles deposited in the absence of liposomes,

219 but otherwise identical experimental conditions, present a spectrum coincident with that of

220 hydroxyapatite with a distinctive sharp peak at 3570 cm^{-1}. Therefore, suggesting that the CaP shell

221 deposited on the liposome surface is amorphous. In line with this observation, XRD (*see* S.I. Fig. S2)

222 and WAXS (see Fig. 3b) diffractograms of CaPLiLX powders and CaPLiLX aqueous suspensions,

223 respectively, show broad and diffuse patterns characteristic of non-crystalline phases. Furthermore, no

224 diffraction patterns were observed in HR-STEM images.[24–26]

225

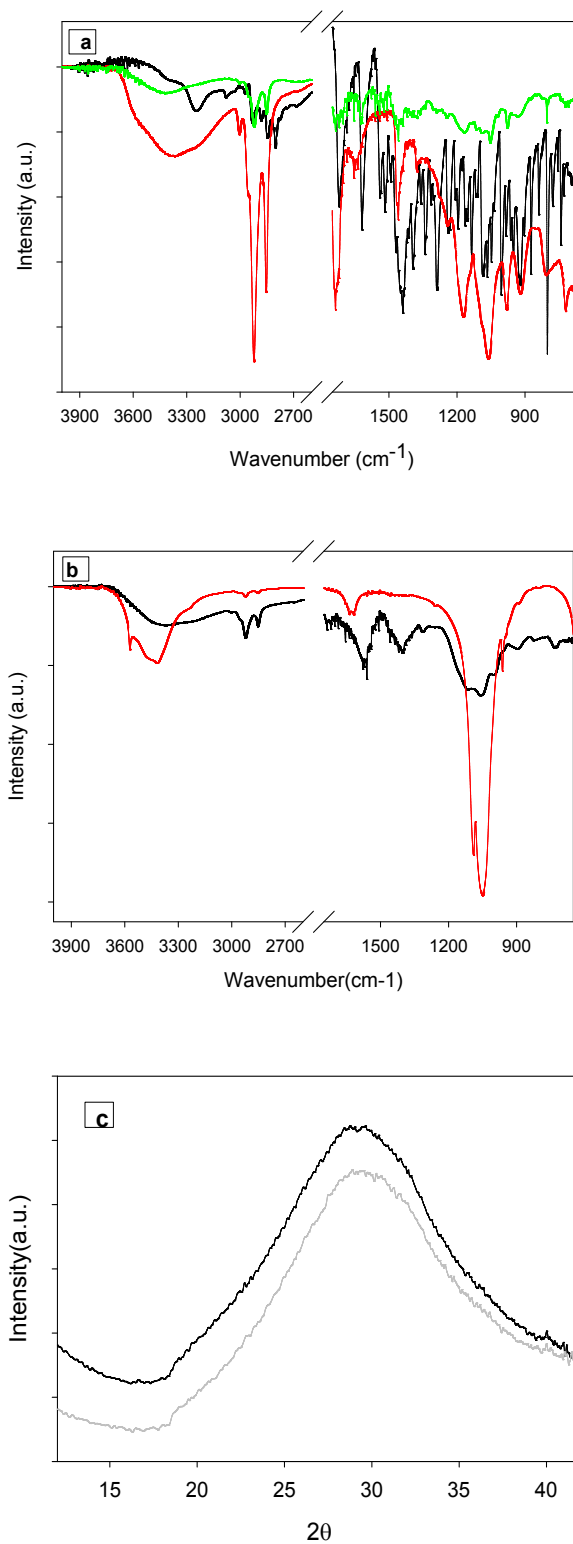New Journal of Chemistry Accepted Manuscript

Fig. 3. (a) ATR-FTIR absorption spectra of LX (black), DOPA (red) and LiLX (green). (b) ATR-FTIR absorption spectra of CaPLiLX (black) and CaP deposited in the absence of liposomes (red). (c)

11

249 WAXS patterns obtained from CaPLiLX colloidal suspensions in the absence (black line) and in the

250 presence (grey line) of 0.05 M of Ca^{2+} ions.

251 Two experimental conditions favored the precipitation of an amorphous CaP (ACP) shell. On one hand,

252 the Ca/P molar ratio added to the liposomes in order to deposit the CaP shell is 1.0, without considering

253 the lipids phosphate head groups. This ratio is in the lower limit range of $1 - 2.2$ reported for

254 amorphous phases.[26] On the other hand, the presence of organic compounds (such as lipids) diminish

255 the solubility of ions due to a change in the dielectric constant of the media.[26] An increase in

256 precipitation kinetics of Ca^{2+} and PO_4^{3-} may occur, which favors amorphization. The amorphous phase

257 was further stabilized by surface derivatization with CEPA.

3.2 Determination of liposome and encapsulated LX concentrations.

259 Liposomes encapsulation of LX, as evaluated from LX absorption at 290 nm, growths with increasing

260 solution concentration of LX up to 100 μM. Higher LX concentrations do not lead to an increased

261 loading of the antibiotic. A minimum LX *encapsulation efficiency* of 56.5% was obtained for LX

262 solution concentrations of 100 μM, of the order reported for LX encapsulation in nanostructured

263 myristyl myristate lipid particles employing sonication methods [27] and for that obtained in soya

264 lecithin/cholesterol synthesized by the so-called remote loading methods.[18]

265 To calculate approximately the total number of liposomes in suspension, the volume of a lipid molecule

266 was estimated considering the approximation postulated by Koenig for unsaturated

267 phosphatidylcholine lipids in the liquid crystalline lamellar phase. The equation $V_L(T) = V_H + n_{CH}x$

268 $V_{CH}(T) + n_{CH2}xV_{CH2}(T) + n_{CH3}xV_{CH3}$ was used to estimate a volume of ~1300 $Å^3$ for a DOPA

269 molecule, where n_{CH}, n_{CH2} and n_{CH3} are the number of carbons in double bonds, methylene-, and methyl

270 groups respectively; and V_{CH}, V_{CH2}, and V_{CH3} are the respective Koenig segmental volumes.[28]

271 Considering that CaPLiLX size is in the range from 90 to 160 nm (as observed by TEM), that the

272 thickness of CaP coating ranges from 20 to 40 nm [10] and the thickness of a bilayer is of ~4 nm, [29,30] a

273　simple geometrical calculation yields a bilayer volume of about 2.6×10^7- 7.0×10^7 $Å^3$ for a liposome

274　carrying the antibiotic LX. Therefore, each liposome is composed by *ca*. 2.0×10^4 to 5.4×10^4 DOPA

275　molecules equivalent to 2.4×10^{-14}- 6.5×10^{-14} mg DOPA. Since 1 mg of DOPA molecules were

276　contained in 1 mL suspension of liposomes (*see above*), a concentration in suspension of 1.5×10^{13} -

277　4.2×10^{13} liposome/mL is retrieved. Considering an encapsulated LX concentration of ~3.3 µg per ml

278　of liposome suspension after coating, then an estimate of 7.9×10^{-14}- 2.2×10^{-13} µg LX/ liposome is

279　obtained.　Therefore, the minimal bactericidal concentration (MBC) of free LX needed to treat *S.*

280　*aureus* strains (∼1.0 µg/mL) (*see below*) is contained in ~ 8.8×10^{12} CaP-coated liposomes, that is *ca*.

281　40 % of the liposomes contained in 1 mL suspension.

282　The calcium concentration in the CaPLiLX suspension determined by ICP-OES was of 34.5 mg/kg

283　(~34.5 µg/mL). Considering that all the liposomes are covered by the CaP shell and no calcium

284　phosphate phase is formed separately (*vide supra*), about 8.2×10^{-13} -2.3×10^{-12} µg Ca/liposome can be

285　estimated. Considering that the mineral phase is composed of amorphous dicalcium phosphate

286　dyhydrate (DCP,$CaHPO_4.2H_2O$), of 2.31 gr/cm^3 density[31] a volume of 1.5×10^6 -$4.3\times10^7 Å^3$ is

287　calculated for the nanoshell from which a thickness of ~10 nm can be estimated, in good agreement

288　with that observed in TEM images of empty CaPLi.[10]

289

3.3 Localization of the drugs within the liposome structure.

291　LX emission spectrum obtained from CaPLiLX aqueous suspensions upon 340 nm excitation (see Fig.

292　4a) is very broad, suggesting the localization of LX in different environments. In fact, a bilinear

293　analysis suggests the contribution of three well differentiated emitters, denoted as E1, E2, and E3 with

294　16, 60 and 24 % contribution to the overall emission, respectively. The emission spectra of E1

295　(maximum emission at 430 nm) and E2 (maximum emission at 455 nm), see Fig. 4a, are in complete

296　agreement with those obtained by TRES analysis for decay times of 1.7 ns and 6.5 ns, respectively.

297　The E2 emission maxima and corresponding lifetime are in excellent agreement with those of LX

298 aqueous solutions of pH 7.4 showing an emission maximum (λ^{em}_{max}) at 460 nm with decay lifetime

299 τ_{aq} of (6.2 ± 0.1) ns upon 341 nm excitation as also shown in Fig. 4a. E1 emission spectrum and decay

300 lifetime are similar to those observed in a less polar media like hexane (τ_{hexane} = (1.4 ±0.1) ns and λ_{max}

301 425 nm, see Fig. 4a), in line with the fact that hexane might resemble the low polarity environment of

302 the DOPA bilayer. The third component, E3, with an emission maximum at 495 nm may be attributed

303 to the protonated levofloxacin molecule, LXH^+ [32] though an adsorbed specie on the CaP interface [33]

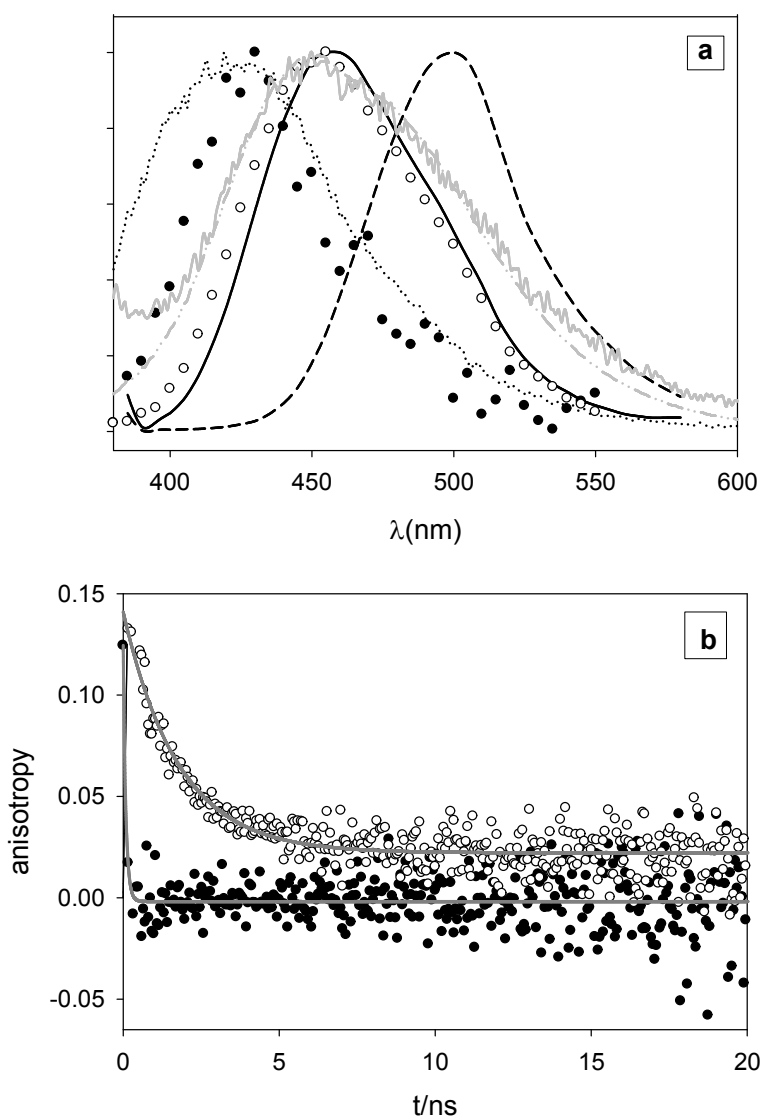304 and binding to divalent cations [34] cannot be discarded.

305

306 **Fig. 4.** (a) Emission spectra of: CaPLiLX aqueous solutions upon 341 nm excitation (grey solid lines)

307 and fitting to three components (grey dashed lines); LX aqueous solutions of pH 7.4 (black solid line)

308 and pH 4(black dashed line); LX in hexane (black dotted line); emitting specie E1 (●) and emitting

309 specie E2 (○). (b) Time-resolved fluorescence anisotropy decay LX (λ_{exc} = 341 nm) in aqueous media

310 (●) and encapsulated in liposomes (○). The grey lines stand for the monoexponential fitting, see text.

311

312 Time resolved anisotropy experiments of LX and LiLX aqueous suspensions were performed upon

313 341 nm excitation. The time-resolved anisotropic decays could be well fitted to a monoexponential

314 decay for both samples as shown in Fig. 4b. The rotational correlation times obtained for LX and LiLX

315 samples are θ_{LX}=0.08 ± 0.09 ns and θ_{LiLX}=1.8 ± 0.5 ns, respectively. From these values and considering

316 spherical species, [35] hydrodynamic radius (r_h) of 4.5 and 12.5 Å were estimated for LX and LiLX,

317 respectively. While the value obtained for LX in aqueous solutions is of the order expected for small

318 organic molecules, that obtained for LX encapsulated in the liposome suggests a motional restriction

319 as also reported for norfloxacin in AOT reverse micelles.[36]

320 Altogether, the previous results support LX localization within the liposome, with a preferential

321 location in the liposome aqueous core and minor amounts located within the lipid bilayer of the

322 liposomes and adsorbed to the CaP shell. A similar distribution was reported for ciprofloxacin in L-

323 α-1, 2-Dipalmitoyl-sn-glycerophosphocholine liposomes.[37]

324

3.4 Drug release profiles in aqueous media as a function of pH and ions- containing media.

326 Release profiles of free LX in aqueous solution from membrane bags immersed in PBS occurs almost

327 completely in less than 3 hours under conditions of constant stirring and ionic strength of 0.16 M and

328 pH 7.4, as shown in Fig. 5 *inset*. However, in acetate buffer solution of I=0.009 M and pH 4.35, the

329 drug was completely transferred to the media in less than one hour (see SI, Fig. S3). Thus, these

330 observations suggest that diffusion outside the dialysis membrane may limit LX release studies from

331 CaPLiLX for liberation times of a few hours, depending on the release media.

15

332 Encapsulated drug in CaPLiLX vesicles in PBS, acetate buffers and SBF media (see Fig. 5) showed a

333 fast-initial drug release of *ca.* 35-45% in all the studied media during the first hours. This burst release

334 is coincident with that observed for a sample of LX adsorbed in the outer layer of empty liposomes in

335 PBS media.[33,38,39] Since the burst release takes place in the same time window than diffusion of LX

336 from the dialysis membrane as may be observed in Fig. 5(*inset*) for experiments in PBS, care should

337 be taken in the analysis of the drug release mechanisms from these experiments.

338 To obtain some information on the mechanisms involved, the fraction of drug released at time t (RR)

339 up to RR= 0.6 of all curves in Fig. 5 were fitted to Korsmeyer-Peppas (KP) model developed on the

340 basis of water-soluble drug release from polymeric matrices and also applied to porous CaP-ceramic

341 materials and composites.[40,41] To that purpose, curves of RR *versus* time were fitted (see lines in Fig.

342 5) to the relation $RR = k_{KP} \times t^n$, where k_{KP} is the release rate constant which depends on the structural

343 and physical characteristics of the carrier and the drug, and *n* is the release exponent which depends

344 on the drug release mechanism and on the carrier geometry. The fitted parameters are displayed in SI

345 Table S1. Obtained k_{KP} values are, within the experimental error, similar for surface adsorbed LX in

346 CaPLi and CaPLiLX, both, in PBS (pH 7.4) and acetate (pH 4.35) buffers, thus supporting the same

347 nature of the vehicle in all cases. On the other hand, values of the diffusional exponent *n* were, within

348 the experimental error, of *ca.* 0.11 for all experiments. Considering that values of *n* = 0.43 are reported

349 as the limiting value for a Fickian diffusion mechanism from monodispersed spherical samples,[42] the

350 lower values of *n* observed here may be partly related to the size distribution polydispersity of the

351 particles which leads to an accelerated release process at short times and a decelerated transport at long

352 times.[42] Interestingly, dialysis of free LX show $k_{KP} = 0.59$ different from that of CaPLi and CaPLiLX,

353 and *n*=0.6 ± 0.1 which is related to a typical diffusional mechanism.

354 Altogether, these results further support that, any LX release form CaPLiLX vesicles in PBS and

355 acetate buffers occurs from adsorbed LX on the CaP outer shell of the nanostructure. Such drug release

356 occurs within the same time window of solvent free LX diffusion out of the dialysis membrane.

357   Considering that, after the first burst no further LX release is observed from CaPLiLX in PBS and

358   acetate buffers and since liberation of surface adsorbed LX from CaPLi is complete in this time

359   window, it may be concluded that surface adsorbed LX on the vehicle outer shell accounts for a 40 to

360   45 % of total LX contained in CaPLiLX.

361   A different situation is observed for CaPLiLX in SBF where a preferential drug release of *ca.* 90%

362   drug after 50 hs is observed, thus indicating that SBF ionic composition is responsible for the improved

363   release. Also, k_{KP} = 0.55 obtained in SBF (pH 7.4) similar to that of solvent free LX, seems to support

364   an alteration in the nanocarrier facilitating the delivery of the drug.

365

366
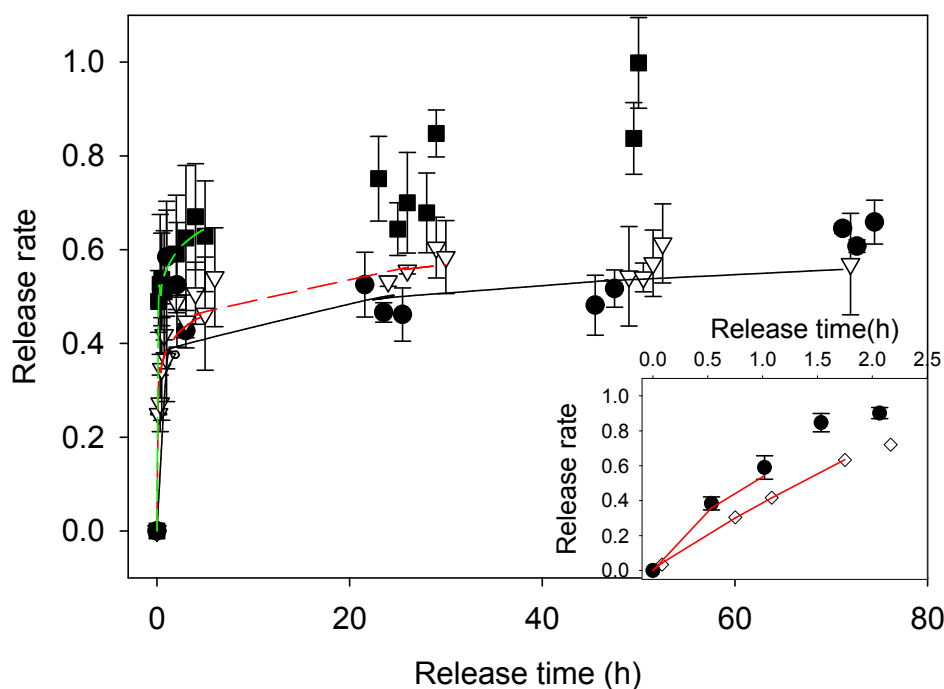
Fig. 5. Release profiles for LX entrapped in CaPLiLX in PBS (black circles), acetate buffer solution

368   (white triangles) and SBF (black squares). Curves stand for the fitting to Kosmeyer-Peppas model (up

369   to *ca* 0.6). *Inset*: Release of LX adsorbed in empty CaPLi in PBS (black diamonds) and solvent free

370   LX diffusion out of the dialysis membrane in PBS (white diamonds). Red curves stand for the fitting

371   to Kosmeyer-Peppas model (up to *ca* 0.6). Error bars stands for SD.

3.5 Proving the release mechanism in SBF.

Considering the amorphous character of the CaP coating as determined by XRD experiments, we hypothesized that the presence of Ca^{2+} and Mg^{2+} ions in SBF may be involved in the improved drug release from the nanocarriers. In a first instance, the transformation of the amorphous calcium phosphate (ACP) to crystalline apatite in the presence of Ca^{2+} and Mg^{2+}, in line with the reported transformation of amino acid containing amorphous calcium phosphates into apatite when immersed in calcium containing solution,[43] was explored by XRD and WAXS.

The XRD pattern (Fig. S2) obtained for CaPLiLX deposited on a glass slide from a solution containing Ca^{2+} (as $CaCl_2$ 0.05 M) is coincident with that obtained in the absence of the divalent ion salt. Both samples present a broad band at 2θ~25ºC typical of an amorphous sample. Also, WAXS experimental patterns shown in Fig. 3b, present the same broad band in the range 20-40 º typical of amorphous samples, for both CaPLiLX, and CaPLiLX suspended in a Ca^{2+} solution (as $CaCl_2$ 0.05 M). Altogether, XRD and WAXS data confirm that no significant formation of a calcium phosphate crystalline phase occurs when the CaP shell gets in contact with calcium ions.

Formation of a coordination complex between surface carboxyl groups of nanoparticles and Ca^{2+} ions is well-reported in the literature.[44] Considering that our CaP nanoshells are surface-terminated by the attachment of CEPA moieties, carboxyl groups are abundant on the nanoshell surface (*see* ATR-FTIR results). The bonding of Ca^{2+} ions to these carboxyl surface groups may trigger the disassembling of the whole structure leading finally to an improved drug release. In that sense, it was demonstrated that the presence of divalent cations as Ca^{2+} and Mg^{2+} can lead to the collapse of carboxylic terminated brushes of spherical colloids also provoking their aggregation.[45,46] With the purpose of confirming such hypothesis, the hydrodynamic diameter and surface charge of CaPLiLX sample were evaluated in the presence of 0.05M of divalent cations (Ca^{2+} and Mg^{2+}), as depicted in SI, Table S2. An increase of the hydrodynamic diameter of the nanoshells and the consequent decrease in the electrophoretic mobility was observed in the presence of both, Ca^{2+} and Mg^{2+}, supporting the formation of

397 agglomerates mediated by divalent cations-carboxyl complexes.[47] Moreover, a significant increase of

398 PDI (≥ 0.75) was also observed in the presence of divalent cations, which may be caused by increased

399 nanocarrier fusion and aggregation. Considering these results and the enhanced LX release in SBF (*see*

400 *above*), the effect of divalent cations on the agglomeration and consequent disassembling of the

401 nanoshells in solution is strongly supported. In view of these results and bearing in mind the aim to

402 develop a drug nanocarrier responsive to Ca^{2+}-surfaces, we further explored the behavior of the CaP

403 nanoshells over Ca^{2+}- enriched surfaces by diverse microscopy studies.

3.6 Interaction of nanoshell with Ca^{2+} rich surfaces.

405 AFM topographic images of CaPLiLX nanoshells deposited on mica surfaces revealed spherical-like

406 particles and some agglomerates (Fig. 6a). The height profile showed well defined spheres with an

407 average height of 9.8 nm and an average diameter of 132.5 nm, in line with DLS, and electron

408 microscopies results. On the other hand, images of CaPLiLX dropped on mica with the previous

409 deposition of Ca^{2+} (Fig. 6b and 6c) showed the aggregation, crushing and dragging of the nanoshells

410 on the surface. In addition, the irregular shapes registered by the probe are evident in the height profile,

411 for both 5.0 (Fig. 6b) and 1.2 μm (Fig. 6c), where a height of *ca.* 4 nm is displayed, in coincidence

412 with that observed for a phospholipid bilayer thickness.[29,30] The result suggests the rupture of the CaP

413 shell when the sample is in contact with a Ca^{2+} rich surface, leaving the liposomes exposed and leading
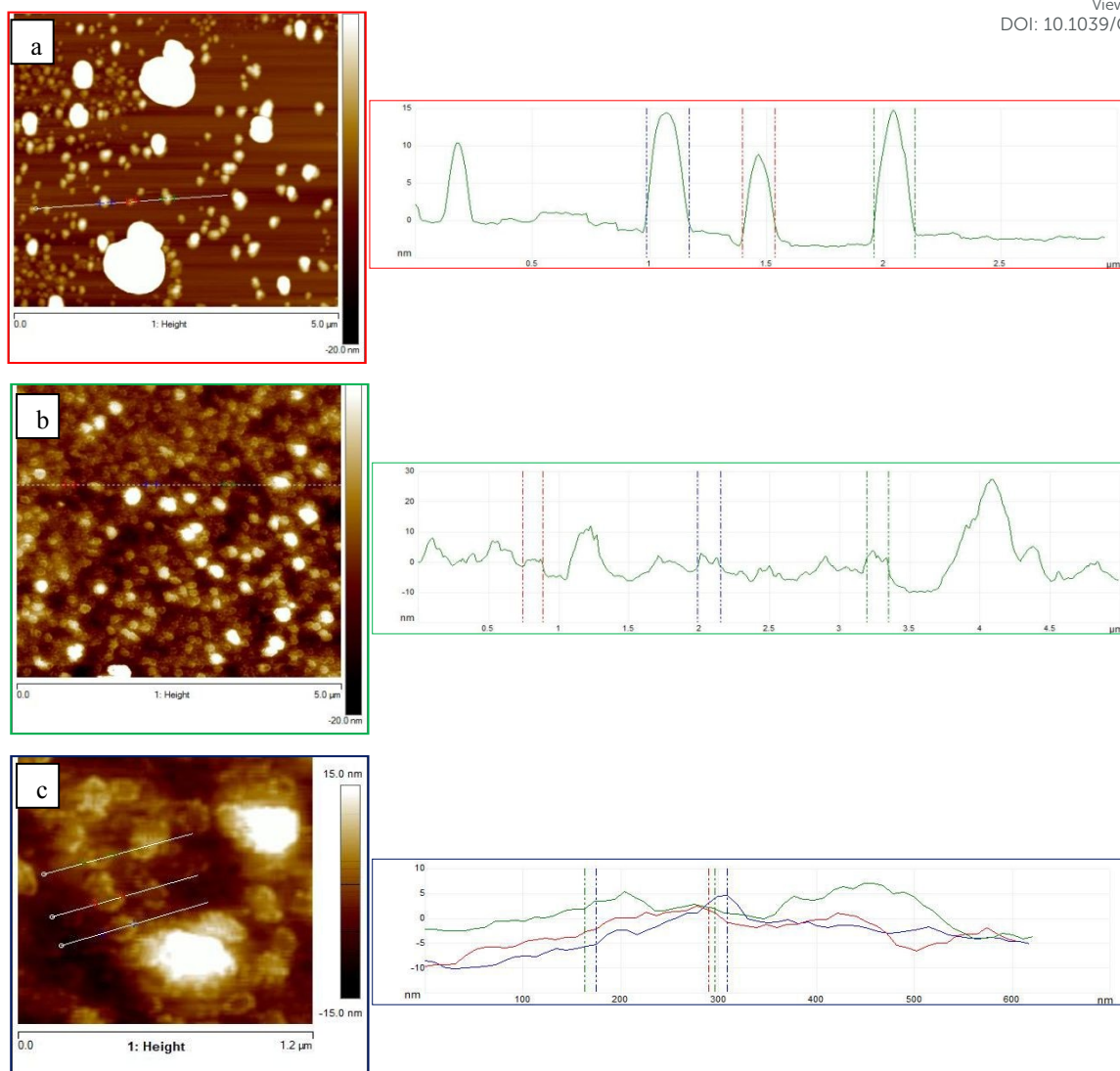
414 to their disruption on the surface.

Fig. 6. AFM images of CaPLiLX on mica (a) and on Ca^{2+} mica modified surface (b and c).

In order to explore the calcium speciation and contact time on the CaP nanoshells interaction with calcium-enriched surfaces, SEM images of CaPLiLX dropped on BGS and Ap-BGS were obtained after 10 and 120 minutes of contact (Fig. 7). Unmodified BGS scaffold's image is also displayed (Fig. 7, *inset*). Although nanoshells were observed on both Ap-modified and BGS unaltered surfaces, a noticeable accumulation of CaPLiLX over Ap-BGS was observed for both contact times. On the other hand, nanoshells observed in the unmodified BGS, showed uniform distribution over the surface. The images taken at different contact times showed the immediate accumulation (10 min) of the nanoshells

447 on the Ap-BGS surface. The results suggest that the nanoshells have an important interaction with

448 apatite-enriched scaffolds and a preferable accumulation is taking place over calcium- modified
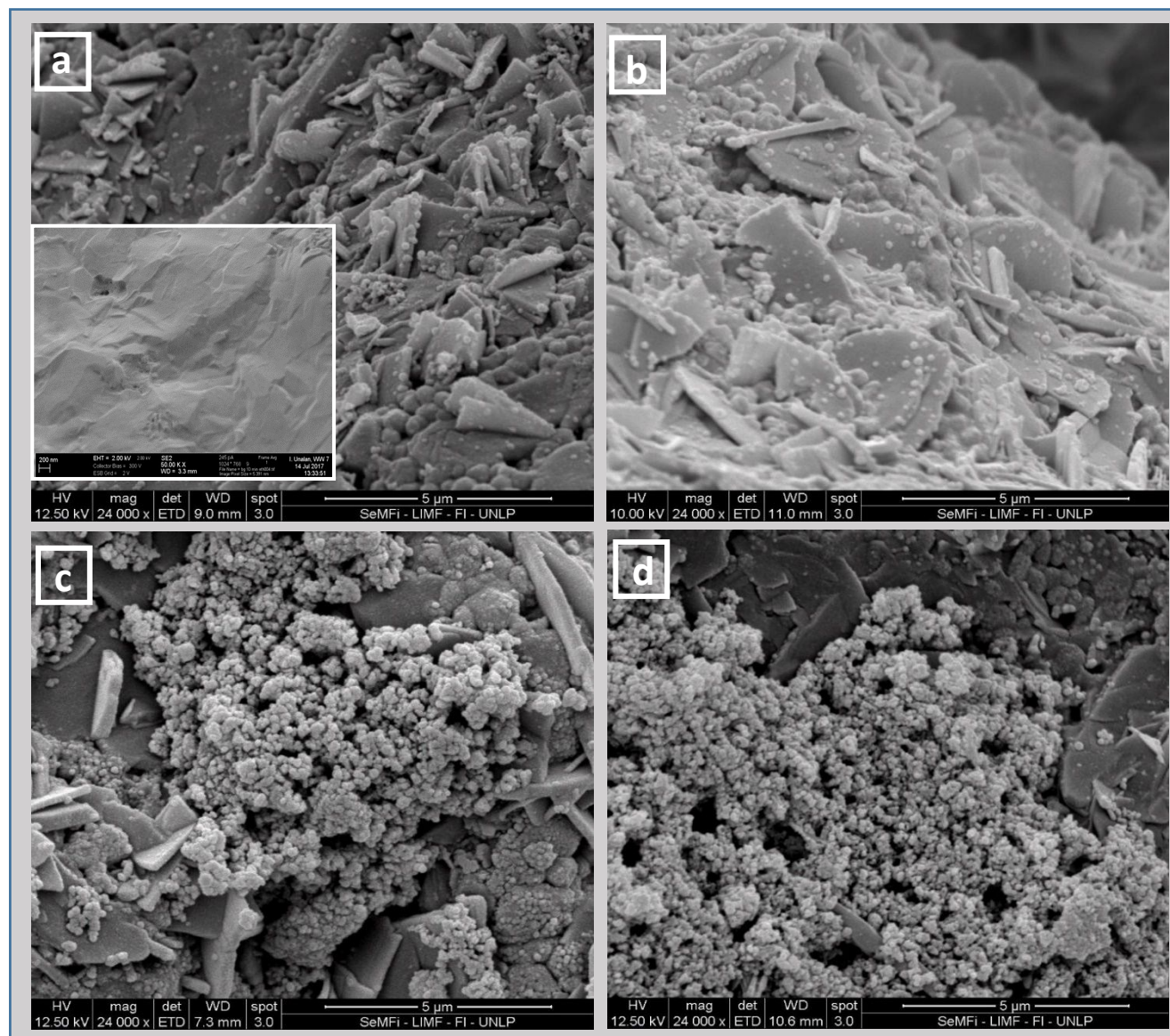
449 surface.

450

Fig. 7. SEM images of (a) CaPLiLX over BGS after 10 min and (b) after 120 min. (c) CaPLiLX over

468 Ap-BGS after 10 min and (d) after 120 min of contact time. *Inset*: Image of unmodified BGS scaffold.

470 Finally, to confirm the release of the content when the CaP nanoshells are disrupted, a new suspension

471 of CaP coated liposomes containing acridine orange fluorophore (CaPLiAO) was prepared and

472 observed in an epifluorescence microscope. The release of acridine orange was studied on uncoated

473 and Ap-coated glass slides observing the morphology and changes in fluorophore emission intensity

474 at different contact times. To that purpose, 2 mL of CaPLiAO suspension was deposited over the

475 glasses and the whole system observed immediately (0 min) and after 10 minutes and 180 min of

476 contact time. Control images were also obtained before adding the CaPLiAO suspension to check the

477 absence of emission in unmodified and Ap-modified glass surfaces. The images, taken in triplicate,

478 showed the release of the AO fluorophore from the CaP nanoshells on the Ap-modified glasses since

479 the first minutes of contact leading to the staining of the entire Ap-modified glass surface after 180

480 min (Fig. 8). On the other hand, the emission observed over the unmodified surface is centered in small

481 areas corresponding to the fluorophore contained in nanoshells or their aggregates.
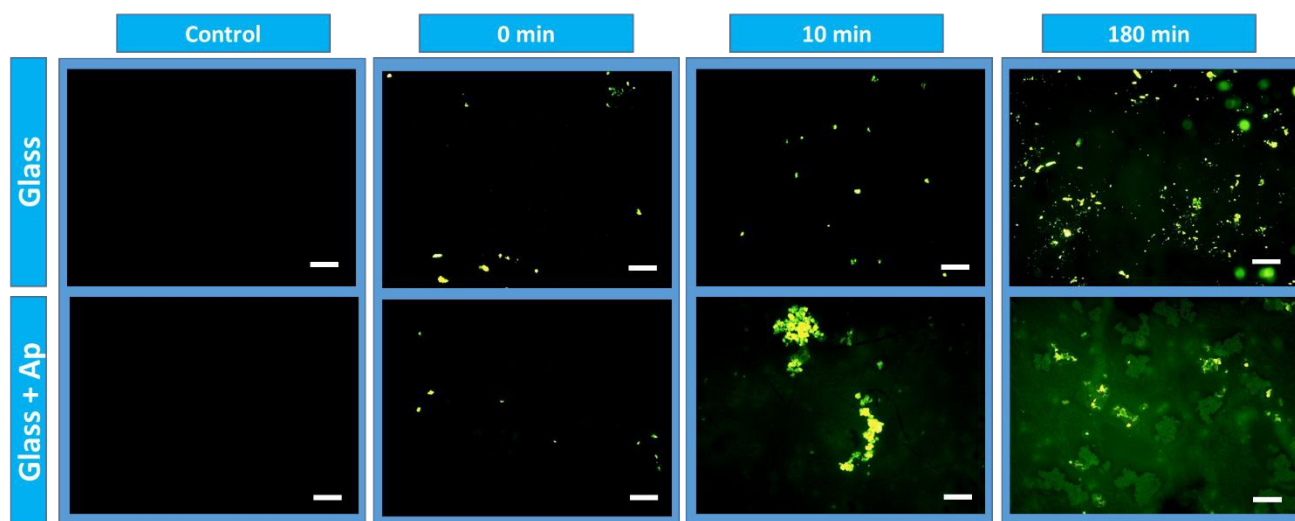

482

483

Fig. 8. Epifluorescence images of CaPLiAO interaction with Ap-modified (below) and unmodified

485 (above) glass at 0 min, 10 min and 180 min of contact time. Control images are also displayed. Scale

486 bar is 10 μm.

487

488 The fluorescence intensity as a function of surface and time was evaluated by calculation of the image

489 covered area using Image J software. The results presented in Fig. S4 clearly demonstrated the

490   enhanced release of the AO fluorophore from the CaP nanoshell deposited over Ap-modified surface

491   as observed by the naked eye.

492   Altogether, atomic force, scanning electron and epifluorescence microscopy results support the

493   hypothesis that the CaP shells accumulate immediately after contact and break over calcium containing

494   surfaces, exposing the liposomes, which are dissembled, releasing their drug content to the

495   surroundings in few hours.

496

497   3.7 Time-kill curve of planktonic *S. aureus*.

498   In order to confirm that the nanoshells are capable of transporting and maintaining the antibiotic

499   activity of encapsulated LX, time-kill curve experiments were performed with LX and CaPLiLX. *In*

500   *vitro* susceptibility of *S. aureus* to LX was determined on planktonic cells. MIC and MBC (see

501   Experimental Section) values obtained for *S. aureus* were 0.5 μg/mL and 1.0 μg/mL, respectively.

502   Based in these results, LX concentration for time-kill assay was evaluated at MBC (2x MIC) value.

503   Time-kill curve for *S. aureus* showed that bactericidal activity was reached at 6 hours and total

504   eradication of bacteria was achieved within 24 h for both free LX and CaPLiLX (Fig. 9). However, a

505   difference was observed in the kinetics of the antimicrobial activity between the CaPLiLX sample and

506   free LX. Although the antimicrobial activity is preserved for the encapsulated formulation, a small

507   difference was observed in the first 3 hours. These results are consistent with the sustained release of

508   LX observed from the nanoshells in solution, reaching about 40 % release in 3h in solution (~1.3 μg

509   LX/mL) (*see* Fig. 5) which explains that both, CaPLiLX and LX solution, exhibited similar

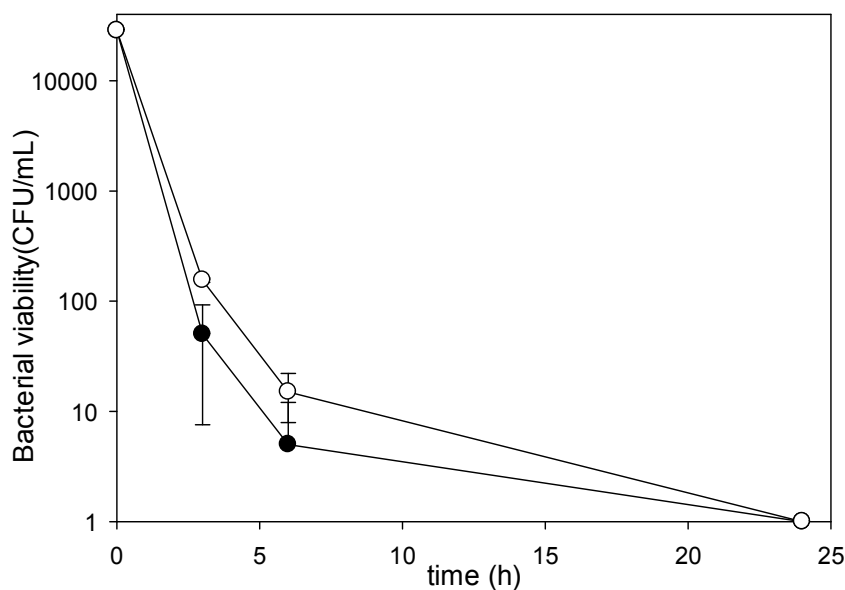510   antimicrobial action against *S. aureus*.

511

23

Fig. 9. Effects of free LX and CaPLiLX on the viability of *S. aureus* ATCC 25923. The *in vitro* time-kill experiments were performed in duplicate; mean and SD values were plotted. 2x MIC LX (●) and CaPLiLX formulation(○). CFU: colony forming unit.

Although the surface charge of the CaPLiLX nanoshell is negative, the nanoshells interact with the *gram-positive* bacterial outer membranes, leading to bacterial killing. This interaction was previously observed for acridine orange and 5,10,15,20-Tetrakis(1-methyl-4-pyridinio)porphyrin containing CaPLi nanoshells.[10] The teichoic acid and the peptidoglycan components of the bacterial cell wall contribute to the negative charge of the staphylococcal cell surface. Moreover, these phosphate-containing and sugar polymers are the major bacterial components for sequestering metal ions from the environment, mostly Ca^{2+} and Mg^{2+}.[48] In our previous work, we hinted that the phosphate groups of the bacterial cell wall and the external calcium and magnesium ions may be responsible for the preferential accumulation of the nanoshells in *S. aureus* biofilms and smears. As was broadly demonstrated in this work, calcium and magnesium ions also play an important role in the agglomeration and consequent disassembling of the nanoshells. We may conclude that the localization of these divalent metal ions on the vicinity of the bacterial wall may attract the nanoshells and finally

529 provoke their disruption and antibiotic content release near the bacterial cell, consistent with our

530 proposed release mechanism.

531

4. CONCLUSIONS

533 Highly stable CaP-coated liposomes of 90 -160 nm size were synthesized and their capability of

534 incorporating model drugs as the antibiotic Levofloxacin demonstrated. The drug distribution inside

535 the aqueous core and into the bilayers was determined by steady state, time resolved and anisotropy

536 fluorescence measurements. Drug adsorption on the CaP surface was also confirmed by release

537 profiles.

538 The amorphous character of the CaP shell of the vehicles is a decisive condition triggering the release

539 of any included and surface adsorbed drug. It is well known from the literature, that amorphous CaP

540 is more easily dissolved than crystalline calcium phosphate solids.[13,49,50] The higher water content of

541 CaP amorphous phase compared to crystalline phases may favor the entrance of the water molecules

542 from the solvent, enhancing its dissolution. Moreover, drug release from the surface of CaP solid

543 nanoparticles depends on the particle phase, the surface impurities, the interaction with water and the

544 nature of the drug. The fast release observed here for adsorbed LX on the surface of CaPLiLX and

545 CaPLi, may be due to a weak adsorption of LX on the amorphous CaP external shell. Whether such

546 burst release is not a desired condition, the dialysis may be a good option for nanoshells purification.

547 Because surface adsorption is involved in the drug inclusion in CaPLi vehicles, other farmaceuticals

548 might show a different behavior, as is the case of the AO dye.[10]

549 The release response of CaP shells to Ca^{2+} and Mg^{2+} cations in solution showed that these divalent

550 ions were able to complex the nanoshell surface provoking aggregation and being able to trigger the

551 disruption of the CaP shell. In line with this behavior, an immediate response of CaP nanoshells

552 localization to Ca^{2+} and hydroxyapatite-modified surfaces was observed, followed by the CaP shell

553 disassembling and fusion of the liposome leading to the release of their content in few hours.

554 Finally, the potential of novel CaP-based nanocarriers for drug delivery applications was demonstrated

555 in bacterial time-kill experiments of *S. aureus* planktonic cells as similar bacterial time-kill curves for

556 CaPLiLX formulations and the free antibiotic were obtained probably as the consequence of the

557 interaction of divalent cations present in the vicinity of the *gram-positive* bacteria with CaPLiLX.

558 Altogether, our work clearly reveals the potential of amorphous calcium organophosphate nanoshells

559 for specific transport, localization and drug delivery to calcium-enriched surfaces, as bone tissues.

ACKNOWLEDGMENTS

ELECTRONIC SUPPLEMENTARY INFORMATION (ESI)

571 Characterization Methods; Electron microscopies images of nanoshells; X-Ray Diffraction patterns

572 of CaP nanoshells; Release profiles for free LX in acetate buffer; Parameters of the fitting of the release

573 profiles to Korsmeyer-Peppas and Weibull model; Diameter and electrophoretic mobility for the

574 nanoshells in the absence and in the presence of Ca^{2+} and Mg^{2+}; Fluorescence covered area on glass

575 slides with added nanoshells as a function of contact time.

REFERENCES

578 1 Y. H. Choi and H.-K. Han, *J. Pharm. Investig.*, 2018, **48**, 43–60.

579　2　J. V Natarajan, C. Nugraha, X. W. Ng and S. Venkatraman, *J. Control. Release*, 2014, **193**, 122–138.

580

581　3　M. Liu, H. Du, W. Zhang and G. Zhai, *Mater. Sci. Eng. C*, 2017, **71**, 1267–1280.

582　4　X. Wang and W. Li, *Nanotechnology*, 2016, **27**, 1–8.

583　5　Y. Zhang, T. Sun and C. Jiang, *Acta Pharm. Sin. B*, 2018, **8**, 34–50.

584　6　C. J. Kowalczewski and J. M. Saul, *Front. Pharmacol.*, 2018, **9**, 1–15.

585　7　Q. Xu, Y. Tanaka and J. T. Czernuszka, *Biomaterials*, 2007, **28**, 2687–2694.

586　8　D. Huang, B. He and P. Mi, *Biomater. Sci.*, 2019.

587　9　H. Y. Erbil, *Surface Chemistry of Solid and Liquid Interfaces*, Blackwell Publishing Ltd, Oxford, First Edit., 2006.

588

589　10　I. Rivero Berti, M. L. Dell' Arciprete, M. L. Dittler, A. Miñan, M. Fernández Lorenzo de Mele and M. Gonzalez, *Colloids Surfaces B Biointerfaces*, 2016, **142**, 214–222.

590

591　11　H. T. Schmidt, B. L. Gray, P. A. Wingert and A. E. Ostafin, *Chem. Mater.*, 2004, **16**, 4942–4947.

592

593　12　C.-H. Yeo, S. H. S. Zein, A. L. Ahmad and D. S. McPhail, *Ceram. Int.*, 2012, **38**, 561–570.

594　13　V. Uskoković and T. A. Desai, *J. Biomed. Mater. Res. - Part A*, 2013, **101 A**, 1416–1426.

595　14　Q. Z. Chen, I. D. Thompson and A. R. Boccaccini, *Biomaterials*, 2006, **27**, 2414–2425.

596　15　M. L. Dittler, I. Unalan, A. Grünewald, A. M. Beltrán, C. A. Grillo, R. Destch, M. C. Gonzalez and A. R. Boccaccini, *Colloids Surfaces B Biointerfaces*, 2019, **182**, 110346.

597

598　16　H. G. Enoch and P. Strittmatter, *Proc Natl Acad Sci USA*, 1979, **76**, 145–149.

599　17　C. J. M. Stewart, *Anal. Biochem.*, 1980, **104**, 10–14.

600　18　X. Zhang, P. Sun, R. Bi, J. Wang, N. Zhang and G. Huang, *J. Drug Target.*, 2009, **17**, 399–407.

601

602　19　P. Wayne, *Performance Standarts for Antimicrobial Disk Susceptibility Tests; Approved Standard; 9 Edition*, 2006, vol. 26.

603

604　20　P. J. Petersen, P. Labthavikul, C. H. Jones and P. A. Bradford, *J. Antimicrob. Chemother.*, 2006, **57**, 573–576.

605

606　21　X.-S. Tao, Y.-G. Sun, X.-J. Lin, L.-L. Hu, T.-Q. Sun, D. Zhang, A.-M. Cao and L.-J. Wan, *Dalt. Trans.*, 2018, **47**, 12843–12846.

607

608　22　E. G. Palacios, A. J. Monhemius and G. Jua, *Hydrometallurgy*, 2004, **72**, 139–148.

609　23　M. Manoj, D. Mangalaraj, N. Ponpandian and C. Viswanathan, *RSC Adv.*, 2015, **5**, 48705–48711.

610

611　24　D. Muthu, M. Gowri, G. Suresh Kumar, V. S. Kattimani and E. K. Girija, *New J. Chem.*, 2019, **43**, 5315–5324.

612

613   25   V. Cadež, D. M. Lyons, D. Kralj and M. D. Sikiri, *Crystals*, 2018, **8**.

614   26   S. V Dorozhkin, *Acta Biomater.*, 2010, **6**, 4457–4475.

615   27   G. A. Islan, P. C. Tornello, G. A. Abraham, N. Duran and G. R. Castro, *Colloids Surfaces B*
616   *Biointerfaces*, 2016, **143**, 168–176.

617   28   B. W. Koenig and K. Gawrisch, *Biochim. Biophys. Acta*, 2005, **1715**, 65–70.

618   29   Z. V. Feng, T. A. Spurlin and A. A. Gewirth, *Biophys. J.*, 2005, **88**, 2154–2164.

619   30   N. Delorme and A. Fery, *Phys. Rev. E - Stat. Nonlinear, Soft Matter Phys.*, 2006, **74**, 3–5.

620   31   C. Holt, P. A. Timmins, N. Errington and J. Leaver, *Eur. J. Biochem.*, 1998, **252**, 73–78.

621   32   A. Polishchuk, T. Emelina, E. Karaseva, O. Cramariuc, V. Chukharev and V. Karasev,
622   *Photochem. Photobiol.*, 2014, **90**, 79–84.

623   33   C. F. Marques, A. C. Matos, I. A. C. Ribeiro, L. M. Gonçalves, A. Bettencourt and J. M. F.
624   Ferreira, *J Mater Sci Mater Med*, 2016, **27**, 1–12.

625   34   V. Uivarosi, *Molecules*, 2013, **18**, 11153–11197.

626   35   J. R. Lakowicz, *Principles of Fluorescence Spectroscopy*, Springer, New York, Third Edit.,
627   2006.

628   36   B. K. Paul, N. Ghosh, A. Tewary and S. Mukherjee, *Proc. Indian Natl. Sci. Acad.*, 2016, **82**,
629   1259–1269.

630   37   J. Hernández-Borrell and M. T. Montero, *Int. J. Pharm.*, 2003, **252**, 149–157.

631   38   G. D. Venkatasubbu, S. Ramasamy, V. Ramakrishnan and J. Kumar, *Biotech*, 2011, **1**, 173–
632   186.

633   39   A. Jain and S. K. Jain, *Chem. Phys. Lipids*, 2016, **201**, 28–40.

634   40   S. Dash, P. N. Murthy, L. Nath and P. Chowdhury, *Acta Pol. Pharm. Drug Res.*, 2010, **67**,
635   217–223.

636   41   U. Gbureck, E. Vorndran and J. E. Barralet, *Acta Biomater.*, 2008, **4**, 1480–1486.

637   42   P. L. Ritger and N. A. Peppas, *J. Control. Release*, 1987, **5**, 23–36.

638   43   N. Ikawa, T. Kimura and T. Sano, *J. Mater. Chem.*, 2009, **19**, 4906–4913.

639   44   A. Ethirajan, U. Ziener and K. Landfester, *Chem. Mater.*, 2009, **21**, 2218–2225.

640   45   A. Ezhova and K. Huber, *Macromolecules*, 2016, **49**, 7460–7468.

641   46   R. J. Nap, E. Gonzalez Solveyra and I. Szleifer, *Biomater. Sci.*, 2018, **6**, 1048–1058.

642   47   D. Li, Z. Fang, H. Duan and L. Liang, *Biomater. Sci.*, 2019, **7**, 2841–2849.

643   48   K. J. Thomas and C. V. Rice, *Biochim. Biophys. Acta - Biomembr.*, 2015, **1848**, 1981–1987.

644   49   V. Uskoković, *J. Mater. Chem. B*, 2019, **7**, 3982–3992.

645   50   V. M. Wu and V. Uskoković, *Biochim. Biophys. Acta - Gen. Subj.*, 2016, **1860**, 2157–2168.

646

Table of Content

We show that amorphous calcium organophosphate nanoshells are prone to agglomerate

and disassemble when Ca^{2+} ions are present in the solution and on surfaces, wich have

great implications for targeting and controlled drug release in Ca-rich environments, such

as bone tissues.